Applied Surface Science 328 (2015) 568–576

Contents lists available at ScienceDirect

Applied Surface Science

journal homepage: www.elsevier.com/locate/apsusc

Enhanced photovoltaic performance of QDSSCs via modifying ZnO photoanode with a 3-PPA self-assembled monolayer

Lili Yang[a,b,*], Gang Chen[a,b], Yunfei Sun[a,b], Donglai Han[c,d], Shuo Yang[c,d], Ming Gao[a,b], Zhe Wang[a,b], Ping Zou[a,b], Hongmei Luan[a,b], Xiangwang Kong[a,b], Jinghai Yang[a,b]

[a] Department of Physics, Jilin Normal University, Siping 136000, China
[b] Key Laboratory of Functional Materials Physics and Chemistry of the Ministry of Education, Jilin Normal University, Siping 136000, Jilin, China
[c] State Key Laboratory of Luminescence and Applications, Changchun Institute of Optics, Fine Mechanics and Physics, Chinese Academy of Sciences, Changchun 130033, China
[d] University of Chinese Academy of Sciences, Beijing 100049, China

ARTICLE INFO

Article history:
Received 5 October 2014
Received in revised form
16 December 2014
Accepted 16 December 2014
Available online 24 December 2014

Keywords:
ZnO nanorods
Quantum dots sensitized solar cells
Self-assembled monolayers
Conversion efficiencies

ABSTRACT

A SAMs layer of 3-PPA with a phosphonic acid headgroup and carboxylic acid tailgroups has been used to modify the surface of ZnO nanorods photoanode in CdS quantum dots sensitized solar cells. Its effects on the photovoltic performance have been investigated in detail by adjusting the concentration and deposition time of 3-PPA. Especially, we utilize ultraviolet photoelectron spectroscopy to characterize the variation of band alignment after introducing 3-PPA layer in the solar cells. The results reveal that the 3-PPA not only suppress the electron-hole recombination process due to its passivation on the surface defects, but forms an energy barrier to efficiently retard the back transfer of electrons, which finally results in the enhancement of conversion efficiency of solar cells.

1. Introduction

Quantum dot-sensitized solar cells (QDSSCs) as derivatives of dye-sensitized solar cells (DSSCs) have attracted considerable attention, since the sensitizer of quantum dots (QDs) exhibits fantastic advantages in comparison with dyes, such as higher extinction coefficients, tunable band gap due to the quantum confinement effect, and the possibility of multiple exciton generation [1–4]. All these advantages are quite beneficial for increasing the exciton concentration, quantum yield and lifetime of hot electrons, which finally results in a higher performance of QDSSCs. However, so far, the highest photoelectric conversion efficiency of QDSSCs is far from 13% of DSSCs [5]. The back electron transfer or recombination processes of photogenerated carriers happened at the interface are known to the main factors for such lower efficiency of QDSSCs. Therefore, how to prevent the back electron transfer or recombination processes and accelerate the transportation of separated charge to the contact electrode is the effective way to improve the efficiency of QDSSCs.

One of popular approach is to deposit a layer of semiconductor or insulator with higher conduction band on the surface of photoanode to form energy barrier, which will effectively retard the back transfer of electrons and strongly enhance the efficiency of QDSSCs [6,7]. For CdS QDs sensitized ZnO nanorods solar cells, people usually introduce ZnS compact layer between ZnO and CdS to retard the back transfer of electrons to the CdS and electrolyte [8,9]. However, to guarantee the crystal quality and accurately control the thickness of ZnS barrier layer, people usually take the methods of chemical vapor deposition and magnetron sputtering, which needs complex process, rigorous experimental conditions and high cost.

As an alternative method, to deposit self-assembled monolayers (SAMs) on the surface of polymer [10,11], metal [12–14] and metal oxide [15–18] is a simple and effective way to control their properties including wettability, work function, and charge transfer, since the SAMs exhibit great advantages such as simple preparation, stable structure, high order and less defects. The SAMs are a two-dimensional molecular array that is spontaneously organized by adsorption of amphiphilic organic molecules on a solid inorganic surface [19]. The SAMs consists of three group: a head group enables the molecule to anchor to a surface; a carbon backbone chain whose length significantly influences the packing density of the SAMs

* Corresponding author at: Department of Physics, Jilin Normal University, No. 1301 Haifeng Street, Siping 136000, China. Tel.: +86 434 3294566; fax: +86 434 3294566.
E-mail address: jhyang1@jlnu.edu.cn (L. Yang).

http://dx.doi.org/10.1016/j.apsusc.2014.12.108
0169-4332/

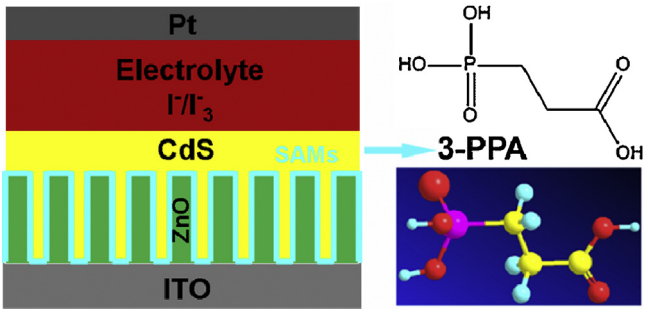

Fig. 1. Device architecture of the QDs solar cell with self-assembled monolayer of 3-PPA modified ZnO. For the molecule formula of 3-PPA as shown in the right-bottom, O, P, C and H atoms are presented by the red, magenta, yellow and light blue color, respectively. (For interpretation of the references to color in this figure legend, the reader is referred to the web version of this article.)

[20,21]; a tail group determines the interfacial properties of the SAMs [22–25]. The SAMs of silanes, thiols, carboxylic acids, and phosphonic acids have all been used in the photovoltaics to modify the transparent electrodes or photoanodes for enhancing the photovolatic performance since they can passivate surface, suppress the surface charge recombination and enhance the charge separation at the interface [26–40]. Beyond that, Wang et al utilized the phosphonic acid SAMs as coadsorbates in dye-sensitized solar cells to improve device efficiencies by the suppression of dark current [26]. Monson et al selected polythiophene and plkanethiol SAMs to modify the interface of ZnO-P3HT bilayer photovoltaic devices and realized the enhancement of photocurrent [28]. However, only a few works so far have been reported about the utilization of SAMs in QDSSCs, and most of them were focused on the TiO_2 photoanode [41–45]. For instance, Bent et al introduced different SAMs between CdS QDs and TiO_2 photoanode and found that the nature of the SAM tailgroup does not significantly affect the uptake of CdS quantum dots on TiO_2 nor their optical properties, and the presence of the SAMs does enhance the power conversion efficiencies almost three times [45]. But they did not reveal the native enhancement mechanism. Since the ZnO photoanodes exhibit better optical and electronic properties than TiO_2, we believe the utilization of SAMs in the ZnO-based QDSSCs may improve their photovoltaic performance as well. However, until now, the reports about effects of SAMs on the performance of ZnO-based QDSSCs is rather rare as well as we know. Therefore, it is quite necessary to do the relative research and reveal the corresponding mechanism.

According to the reports of Pawsey and Folkers, the SAMs with phosphonic acid headgroup could provide the stronger attachment to ZnO [46,47]. Therefore, in this work, we chose 3-PPA with a phosphonic acid headgroup and carboxylic acid tailgroups as SAMs to modify the surface of ZnO nanorods. This 3-PPA/ZnO nanorods was used as photoanode to fabricate CdS QDs synthesized solar cells. Fig. 1 illustrated the schematical structure of the cell. By varying the deposition time of 3-PPA, we investigated in detail the effects of 3-PPA on the surface structure and photovoltic performance of solar cells. In particular, we utilized ultraviolet photoelectron spectroscopy (UPS) to help depict the energy level diagram of solar cells. Then the variation of band alignment will be discussed in detail so that the native function of 3-PPA SAMs will be revealed.

2. Experimental details

2.1. Preparation of vertically aligned ZnO nanorods

The ITO substrates were sequentially cleaned with acetone, alcohol and deionized water for 15 min under ultrasonic treatment. All chemicals (analytical grade reagents) were directly used without further purification. The ZnO nanorods arrays were grown on ITO substrates by two-step CBD method, including a substrate treatment prior to the CBD growth. The detailed process can be found in our previous report [48–50]. In this case, ZnO nanorods arrays were grown in the chemical solution for 6 h under 95 °C.

2.2. Deposition of 3-PPA SAMs

To realize the deposition of 3-PPA SAMs, ZnO nanorods samples were dipped into 10 mM 3-PPA ethanol solutions for 30 s, 1 min, 2 min and 5 min, respectively. The samples were named by 3-PPA(30 s)/ZnO, 3-PPA(1 min)/ZnO, 3-PPA(2 min)/ZnO and 3-PPA(5 min)/ZnO, respectively. After ending the immersion step, the samples were rinsed with ethanol to remove excess 3-PPA molecule. We further prepared another set of samples, i.e. dipping ZnO nanorods into 1 mM, 10 mM and 100 mM 3-PPA solution for 1 min. The samples were named by 3-PPA(1 mM, 1 min)/ZnO, 3-PPA(10 mM, 1 min)/ZnO, 3-PPA(100 mM, 1 min)/ZnO.

2.3. Deposition of CdS QDs

The CdS QDs were in-situ deposited on the surfaces of SAM/ZnO and pure ZnO nanorods by a successive ionic layer adsorption and reaction (SILAR) technique. To complete a SILAR cycle, the ZnO samples were first immersed into $Cd(NO_2)_2$ (0.1 M) solution for 5 min. They were then rinsed with deionized water for 30s to remove excess ions weakly bound to the surface of samples and then immersed in a Na_2S (0.1 M) solution for another 5 min followed by another rinsing with deionized water. These SILAR cycles were repeated about 20 times. Subsequently, the samples were thoroughly washed with ethanol and deionized water and then dried at room temperature for fabricating solar cells.

2.4. Cell fabrication

The photoelectrode consisting of CdS/SAMs/ZnO was incorporated into thin layer sandwich-type cells. A 20 nm platinum-sputtered ITO substrate as the counter electrode and the working electrode were positioned face-to-face. The iodide-based electrolyte, consisting of 1 M LiI and 0.05 M I_2 in alcohol, was injected into the interelectrode space by capillary action.

2.5. Characterization and measurements

The X-ray diffraction (XRD) patterns were recorded by a MAC Science MXP-18 X-ray diffractometer using a Cu target radiation source. The scanning electron microscope (SEM, S-570, Hitachi) was used to characterize the morphology of ZnO nanorod arrays. Transmission electron micrographs (TEM) and high-resolution transmission electron microscopy (HRTEM) images were taken on JEM-2100 transmission electron microscope. X-ray photoelectron spectra (XPS) were recorded on a VG ESCALAB Mark II XPS using Mg $K\alpha$ radiation ($h\nu$ = 1253.6 eV) with a resolution of 1.0 eV. Fourier transform infrared (FT-IR) spectrum was recorded on a Bruker Vertex 70 spectrophotometer in KBr pellets. The photoluminescence (PL) measurements were performed on the Renishaw invia spectroscopy excited by a continuous He–Cd laser with a wavelength of 325 nm at a power of 2 mW. The Ultraviolet–visible (UV–vis) absorption spectra of each photoelectrode were recorded on a UV–vis spectrophotometer (UV-5800PC, Shanghai Metash Instruments Co., Ltd) at room temperature. The photocurrent dependence on the voltage (I–V) were measured under AM 1.5 G simulated sunlight illumination (100 mW/cm^2, Model 91160, Oriel). The performance of ultraviolet photoemission spectroscopy (UPS) was

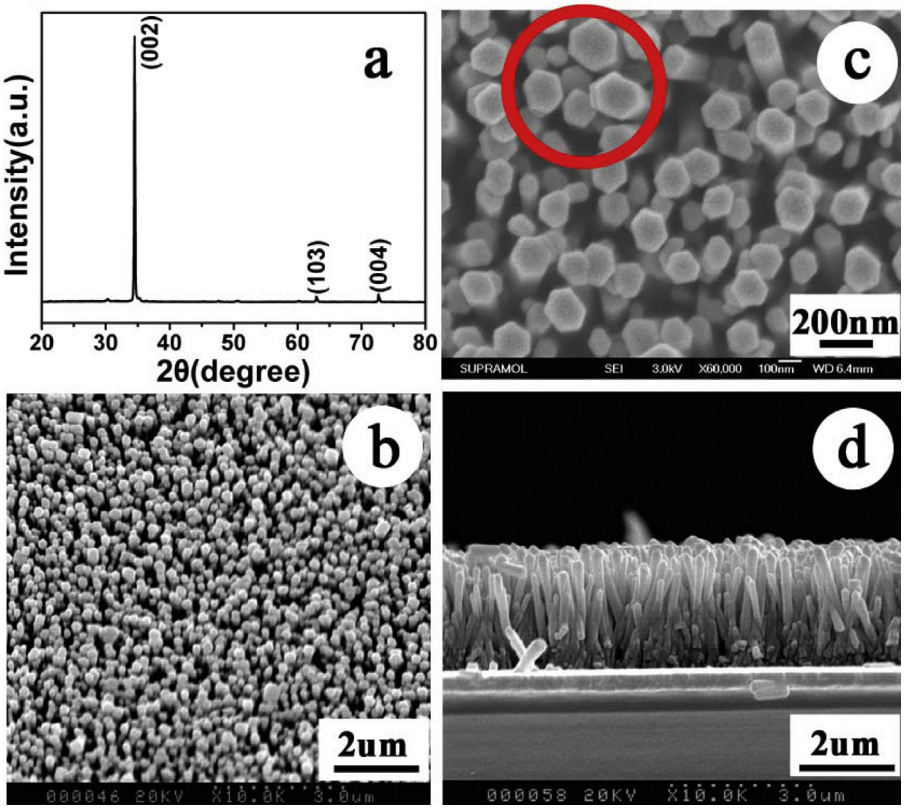

Fig. 2. (a)XRD pattern of the ZnO nanorods arrays; (b) Top-view,(c) magnified top view and (d) cross-sectional SEM images of the ZnO nanorods arrays.

carried out with a helium discharge lamp ($h\nu$ = 21.22 eV) in normal emission with a sample bias of −8 V.

3. Results and discussions

The XRD pattern of the as-grown ZnO nanorods is displayed in Fig. 2(a). All the observed diffraction peaks can be indexed to a wurtzite hexagonal-phase of pure ZnO (JCPDS card, No. 80-0074), which indicates no other impurity phase exists in the samples. Since the (0 0 2) diffraction peak in the XRD pattern turned out to be the dominant one in comparison with the standard pattern of ZnO, we can deduce that the ZnO nanorods are preferentially oriented in the *c*-axis direction [51]. The SEM image in Fig. 2(b) illustrates that the vertically aligned ZnO nanorods uniformly cover the entire ITO substrate with high density. The magnified SEM image in Fig. 2(c) shows that the average diameter of ZnO nanorods is around 150 nm. From the red mark range, we can clearly see that the top of nanorod is hexagonal shape, which is consistent with the XRD results. The cross-sectional SEM image in Fig. 2(d) clearly shows that ZnO nanorods are vertically aligned on the ITO substrates with the length of about 2.7 μm.

To observe the morphology variation after depositing 3-PPA SAMs, the detailed microscopic structure were characterized by TEM technique. Fig. 3(a), (c) and (e) presents the TEM images of ZnO nanorod, 3-PPA(1 min)/ZnO and 3-PPA(5 min)/ZnO, respectively, which clearly shows that the average diameter of these samples is ∼150 nm. From Fig. 3(c) and (e), we can see that the surface of ZnO nanorods became rough after depositing 3-PPA for 1 min and 5 min. Fig. 3(b), (d) and (f) shows the HRTEM images of ZnO nanorods, 3-PPA(1 min)/ZnO nanorods and 3-PPA(5 min)/ZnO nanorods, respectively, in which the well-resolved lattice fringe spacing for these samples can be distinguished to be 0.26 nm, corresponding to the typical wurtzite structure of ZnO. Moreover, from Fig. 3(d), we can observe a thin amorphous layer with 2.2 nm thickness on the surface of ZnO nanorods. From Fig. 3(f), we can see that the thickness of thin amorphous layer on the surface of ZnO nanorods increase to 3.5 nm. Since the thickness of 3-PPA SAMs should increase with prolonging the deposition time, we deduce that this thin amorphous layer appeared in HRTEM images should be originated from 3-PPA SAMs.

To further testify this deduction from TEM results, we use XPS technique to investigate the surface chemical composition of ZnO and 3-PPA(1 min)/ZnO. Fig. 4(a) shows the XPS survey spectra obtained from ZnO and 3-PPA(1 min)/ZnO, in which all of the peaks can only be ascribed to Zn, O, C and P elements. We would like to mention that, for all XPS spectrum in Fig. 4, the binding energies have been calibrated by taking the carbon C 1s peak (285.0 eV) as reference. As reference, we present the high resolution scans of C 1s and O 1s XPS spectra from the ZnO nanorods in Fig. 4(b) and (c), respectively. All of them were deconvoluted into several components by the XPSpeak curve-fitting procedure. From C 1s XPS spectra in Fig. 4(b), we can only obtain a strong peak at 284.6 eV and a weak peak at 288.5 eV, which can be ascribed to the C—C/C—H and O—C=O groups, respectively. These groups are origined from the growth solution or external circumstances. For O 1s XPS spectra in Fig. 4(c), the deconvolutions show the presence of two different O 1s peaks in the ZnO nanorods. The dominant peak centered at 530 eV is associated to the O^{2-} ion in the wurtzite structure surrounded by the Zn atoms with their full complement of nearest-neighbor O^{2-} ions [52]. The peak at 531 eV is attributed to the presence of OH bonds, i.e. ZnO(OH) [52]. To further analyze the surface composition of 3-PPA/ZnO nanorods, the high resolution scans of C 1s, O 1s, Zn 2p and P 2p XPS spectra from 3-PPA/ZnO nanorods are shown in Fig. 4(d)–(g). Fig. 4(d) shows the C 1s XPS spectrum of 3-PPA/ZnO nanorods. The deconvolutions indicate the presence of three different C 1s species in the sample, i.e. the carbon of the aliphatic chain

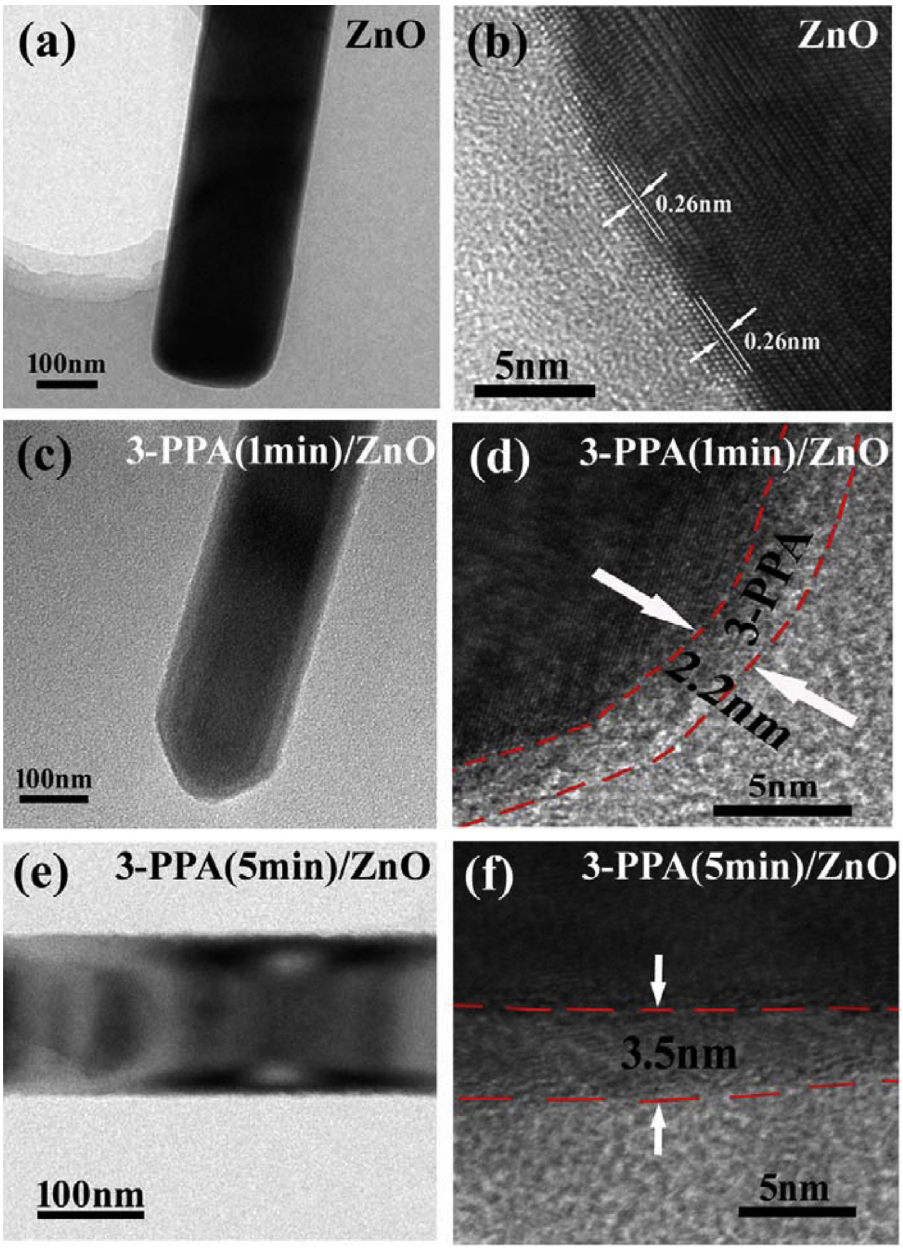

Fig. 3. TEM images of ZnO (a), 3-PPA(1 min)/ZnO (c) and 3-PPA(5 min)/ZnO (e), and HRTEM images of ZnO (b), 3-PPA(1 min)/ZnO (d) and 3-PPA(5 min)/ZnO (f), respectively.

(C—C/C—H) located at 284.51 eV [53], the covalently bound carbon that binds to P of the phosphate group (—C—P(O)$(OH)_2$) located at 285.77 eV [54], and the carbon of the carboxyl group (O—C=O) located at 288.43 eV [19]. The XPS spectrum for the O 1s core level line of 3-PPA/ZnO nanorods can be found in Fig. 4(e). The deconvolutions of four fitting curves indicate four oxygen species exist in the sample. The peak located at 529.97 eV can be assigned to the oxygen from zinc oxide(Zn—O) [52]. The peaks located at 531.25 eV and 532.19 eV can be ascribed to the oxygen in the phosphate group of P=O and P—O—H, respectively [54]. The peaks located at 533.05 eV is originated from the oxygen in the carboxyl group (—COOH) [54]. Fig. 4(f) shows the XPS spectrum for Zn 2p core level lines of 3-PPA/ZnO nanorods. The peaks located at 1021.46 eV and 1044.57 eV are corresponding to the binding energy of Zn $2p_{3/2}$ and Zn $2p_{1/2}$, respectively [52]. Fig. 4(g) shows the XPS spectrum for the P 2p core level line of 3-PPA/ZnO nanorods. The peaks at 132.86 eV and 139.18 eV are attributed to the P $2p_{1/2}$ and P $2p_{3/2}$ peak, respectively [55]. According to the molecule formula of 3-PPA shown in Fig. 1, we can deduce that the above element species originate from ZnO and 3-PPA, indicating the surface of ZnO nanorods have been successfully modified by 3-PPA for 3-PPA/ZnO nanorods.

Fig. 5 demonstrates the FT-IR spectra of the ZnO and 3-PPA(1 min)/ZnO. For ZnO sample, the intensity of all peaks in the spectrum are quite weak. The peaks at 2850–2966 cm^{-1} is known as the ν(C—H). The peaks at 3060–3826 cm^{-1} is identical to the presence of hydroxyl stretching vibration ν(OH). From the spectrum of 3-PPA(1 min)/ZnO sample, we can find that the peaks at 3049 cm^{-1} and 1416 cm^{-1} are identical to the presence of hydroxyl stretching vibration ν(OH) and hydroxyl bending stretching δ(OH), respectively, which is originated from 3-PPA according to its molecule formula. In the carbonyl stretching region, Pawsey et al. have reported that the (ν(C=O)) stretch of hydrogen-bonded carboxylic acid groups lie between 1680 and 1710 cm^{-1}, whereas those of free non-hydrogen-bonded carboxylic acid groups lie between 1735 and 1760 cm^{-1} [54]. The ν(C=O) stretch of carboxylic acid dimer is typically found between 1700 and 1720 cm^{-1}, and the ν_{as}(COO—)

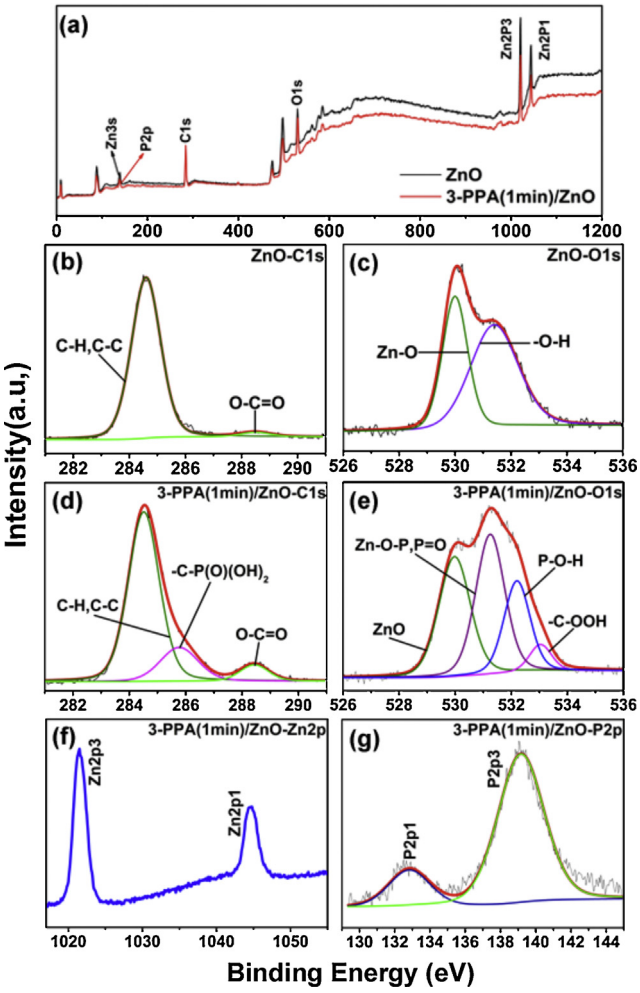

Fig. 4. The XPS spectra of ZnO and 3-PPA(1 min)/ZnO nanorods. (a) Survey spectrum; (b)–(c) is the C 1s and O 1s XPS spectrum of the ZnO nanorods, respectively; (d)–(g) is the C 1s, O 1s, Zn 2p and P 2p XPS spectrum of the 3-PPA(1 min)/ZnO nanorods, respectively.

band at 1540 cm^{-1} can be assigned to the zirconium carboxylate groups of carboxyalkylphosphonic acid-treated ZrO_2 samples [54]. Therefore, in our case, the strong peak located at 1706 cm^{-1} is due to the C═O stretch of the carboxylic group. The peak located around 1569 cm^{-1} can be attributed to the zinc carboxylate groups (ν_{as}(COO—)) [54]. The peaks occurring at 1273 cm^{-1} can be ascribed to C—O stretching in carboxylic groups [53]. We can also observe the characteristic P═O and P—O stretching vibrations in the region between 900 and 1200 cm^{-1} in Fig. 5 [55]. The two characteristic peaks in the region of 945 cm^{-1}–975 cm^{-1} range are originated from P—O—H group [55]. A strong peak

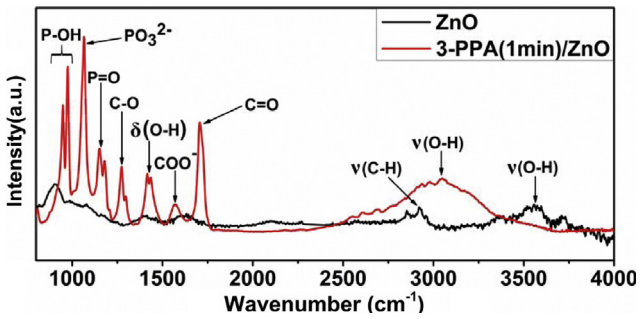

Fig. 5. FT-IR spectra of ZnO and 3-PPA(1 min)/ZnO nanorods.

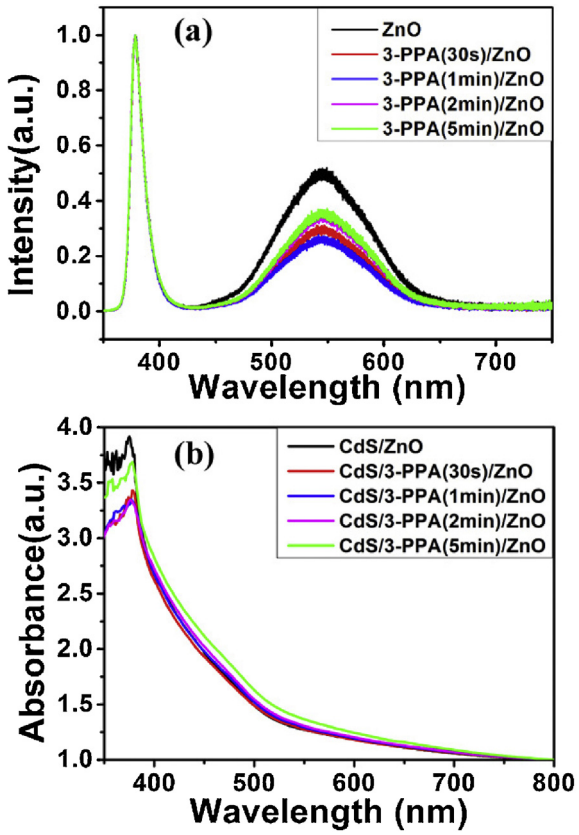

Fig. 6. (a) The photoluminescence spectra of as-grown ZnO and 3-PPA/ZnO nanorods; (b) UV–visible absorption spectra of CdS/3-PPA/ZnO with different deposition time of 3-PPA.

around 1065 cm^{-1} is typically assigned to the stretches of PO_3^{2-} group anchored to the surface through a multidentate bonding [56,57], which involves both P—O and P═O terminations. The peaks occurring at 1151 cm^{-1}–1179 cm^{-1} can be ascribed to the P═O stretching. According to the above assignment to the peaks in the spectra, we can deduce that the POOH and COOH moieties of the 3-PPA are documented on the ZnO nanorods surface, which further proves the results of TEM and XPS [55].

To understand the charge transfer across the interface between CdS QDs sensitizer and ZnO, we performed the room temperature PL measurements on the ZnO nanorods and 3-PPA/ZnO nanorods with depositing 3-PPA for different time (30s, 1 min, 2 min and 5 min). From Fig. 6(a), we can see two characteristic bands in all the PL spectra. One is the UV emission peak located at 378 nm, which corresponds to the near band edge emission of ZnO, namely, the recombination of the free excitons. The room temperature PL peak position can be different, for example, the transition energy from 375 nm to 383 nm, and the exact energy position depends on the contribution between the free exciton and the transition between free electrons to acceptor bound holes [58]. The other is a broad visible light emission (VLE) band in the range of 435–640 nm, which has previously been attributed to the native defects in the crystal structure such as O-vacancy (V_O), Zn-vacancy (V_{Zn}), O-interstitial (O_i), Zn-interstitial (Zn_i), and extrinsic impurities such as substitutional Cu [59].

In order to better compare the intensity of VLE band, we do the normalization according to the UV intensity of bare ZnO nanorods. Clearly, the intensity of VLE firstly decreases and then increases with prolonging the immersion time. When the immersion time is 1 min, the VLE intensity is the lowest, indicating that the defects at the surface of ZnO nanorods have been strongly suppressed due to

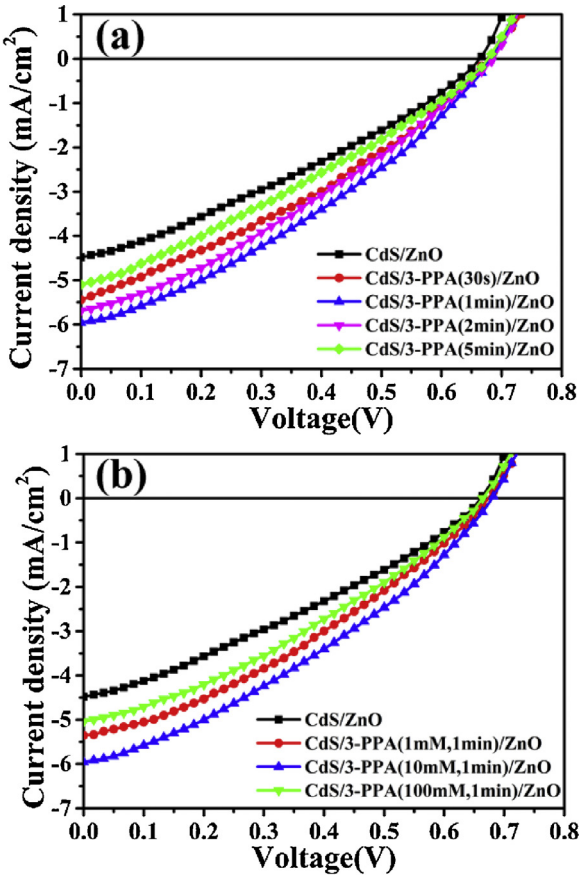

Fig. 7. (a) *I–V* characteristics of CdS/ZnO and CdS/3-PPA/ZnO QDSSCs with depositing 3-PPA in 10 mM solution for different time; (b) *I–V* characteristics of CdS/ZnO and CdS/3-PPA/ZnO QDSSCs with depositing 3-PPA in different concentration solution for 1 min.

the 3-PPA modification since the only difference of these samples is the surface. It is well known that the surfaces of ZnO nanorods grown with CBD method are prone to absorb various kinds of functional groups. According to the chemical reaction in the solution, these functional groups should be related to the elements such as carbon, nitrogen, and hydrogen [59]. After depositing 3-PPA for less 1 min, the rupture Zn—O bond on the ZnO nanorods surfaces are combined with POOH of 3-PPA, which passivate a part of surface defects in ZnO nanorods. When the depositing time reaches up to 1 min, the passivation process was apt to saturated. Once the depositing time is further prolonged, the surface defects will be increased again due to the attachment of excessive 3-PPA.

Fig. 6(b) shows the typical UV–vis absorption spectra of CdS/3-PPA/ZnO with depositing 3-PPA for different time. Interestingly, in comparison with the bare ZnO nanorods, the absolute UV–vis absorbance values just have a little increase even after depositing 3-PPA for 5 min, indicating the deposition of 3-PPA does not significantly influence the uptake of CdS QDs on the ZnO surfaces.

The *I–V* characteristics of all solar cells were carried out under 1.5AM light illumination. The *I–V* curves for CdS/ZnO solar cells and CdS/3-PPA/ZnO solar cells with depositing 3-PPA for different times are displayed in Fig. 7(a). The corresponding performance parameters for each cell are calculated and listed in Table 1, including the short-circuit current density (I_{sc}), the open-circuit voltage (V_{oc}), the fill factor (*FF*), and the photovoltaic conversion efficiency (η). According to the results in Table 1, the best photovoltaic performance comes from the CdS/3-PPA(10 mM, 1 min)/ZnO solar cell, which owns a higher η of 1.36%, I_{sc} of 5.96 mA/cm^2, V_{oc} of 0.680 V and *FF* of 0.336. Compared to the CdS/ZnO solar cell, the η of

Table 1
Photovoltaic parameters obtained from the *I–V* curves of QDSSCs with depositing 3-PPA in 10 mM solution for different time.

Photoelectrodes	J_{sc} (mA/cm^2)	V_{oc} (V)	*FF*	η (%)
CdS/ZnO	4.48	0.663	0.316	0.94
CdS/3-PPA(30s)/ZnO	5.44	0.682	0.321	1.19
CdS/3-PPA(1 min)/ZnO	5.96	0.680	0.336	1.36
CdS/3-PPA(2 min)/ZnO	5.68	0.685	0.316	1.23
CdS/3-PPA(5 min)/ZnO	5.10	0.677	0.301	1.04

CdS/3-PPA(10 mM, 1 min)/ZnO solar cell significant increases from 0.94% to 1.36%. This up to about 45% enhancement of η should be attributed to the increase of both I_{sc} from 4.48 to 5.96 mA/cm^2 and *FF* from 0.316 to 0.336.

Normally, the I_{sc} is mainly dependent on the photocurrent intensity when the solar cell works. The photocurrent density is not only related to the loading amount of CdS QDs on the ZnO nanostructures, but also the process of electron transfer and recombination. As shown in Fig. 7(a), we can see that the efficiencies of the CdS/3-PPA/ZnO solar cells are all higher than that of CdS/ZnO solar cell. According to the UV–vis absorption results shown in Fig. 6(b), we know that the uptake of QDs on the surface of ZnO does not exhibit big variation after depositing 3-PPA SAMs, which indicates the loading amount of CdS QDs is not the factor to influence the I_{sc}. However, from the PL results shown in Fig. 6(a), we know that the deposition of 3-PPA SAMs passivate the surface defects, as a result, the recombination of photogenerated electrons and holes will be greatly suppressed during the transfer process so that more electrons can transmit to the collector electrode, which is one of the reasons for the increase of I_{sc}. In addition, we find that the increase of 3-PPA immersing time greatly influences the photovoltic performance of solar cells. With the increase the immersing time, the photovoltaic conversion efficiency firstly increases and then decreases again. We deduce that this variation tendency maybe related to the degree of saturation for 3-PPA attaching on the surface of ZnO nanorods. When the immersing time is 1 min, the attachment of 3-PPA is apt to saturated so that it can strongly passivate the surface defects and then suppress the recombination of electrons and holes, which finally results in the best photovoltic performance of solar cells. However, when the immersing time further increase to 2 min until 5 min, the photovoltaic performance of the CdS/3-PPA(10 mM, 5 min)/ZnO turns poor again, which may be attributed to the excessive attachment of 3-PPA, since it not only increases the thickness of 3-PPA to hinder the transmission of photoelectrons from CdS to ZnO, but also brings in more surface defects to trap more photogenerated carriers and enhance the electronic–hole recombination.

To further study the effects of 3-PPA layer on the photovoltaic performance of solar cells, another set of CdS/3-PPA/ZnO solar cells with depositing 3-PPA for 1 min in different concentration solution (1 mM, 10 mM and 100 mM) are fabricated. The corresponding *I–V* curves and calculated performance parameters are displayed in Fig. 7(b) and Table 2. We can see from Fig. 7(b) that the best photovoltaic performance is exhibited when the concentration of 3-PPA solution is 10 mM. Moreover, the concentration of 3-PPA obviously affects the photovoltaic performance. We believe that the increase of 3-PPA concentration strongly increase the thickness of SAMs on

Table 2
Photovoltaic parameters obtained from the *I–V* curves of QDSSCs with depositing 3-PPA in different concentration solution for 1 min.

Photoelectrodes	J_{sc} (mA/cm^2)	V_{oc} (V)	*FF*	η (%)
CdS/ZnO	4.48	0.663	0.316	0.94
CdS/3-PPA(1 mM, 1 min)/ZnO	5.35	0.673	0.336	1.21
CdS/3-PPA(10 mM, 1 min)/ZnO	5.96	0.680	0.336	1.36
CdS/3-PPA(100 mM, 1 min)/ZnO	5.04	0.664	0.331	1.11

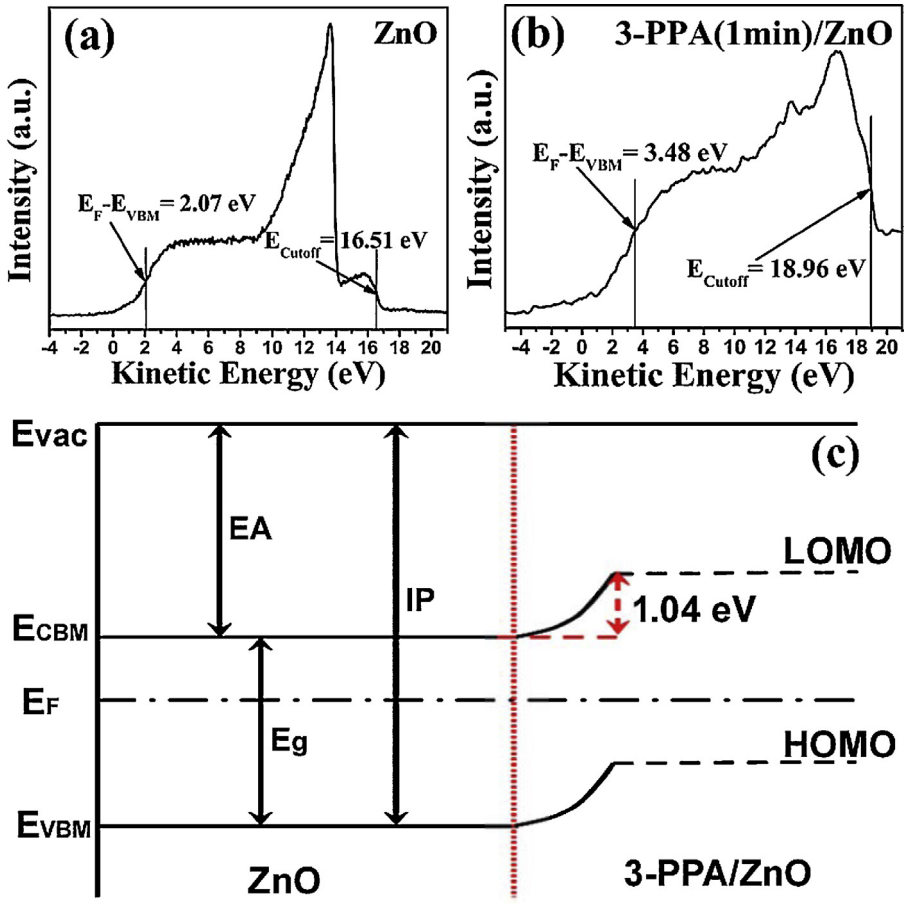

Fig. 8. (a) and (b) show the typical He I ($h\nu$ = 21.22 eV) UPS spectrum of ZnO and 3-PPA/ZnO taken with −8 V bias applied to the sample. (c) Various energy levels near the valence region and its corresponding relationship. E_{vac} is the vacuum level. E_{CBM} and E_{VBM} are the conduction-band minimum and the valence-band maximum, respectively. Definitions of the energy gap (E_g), the ionization potential (IP), and the electron affinity (EA) are also shown.

ZnO surface and results in the lower efficiency of the solar cells, which further testify the results of Fig. 7(a).

To investigate the reproducibility of the CdS/3-PPA DSSCs, we assemble several CdS/3-PPA(10 mM, 1 min)/ZnO QDSSCs, which named the sample 1 (S1), sample 2 (S2) and sample 3 (S3). The relevant photovoltaic parameters are listed in Table 3. We can see that the conversion efficiency is about 1.36%, which indicates the CdS/3-PPA QDSSCs is reproducible.

Besides the suppression of recombination, the SAMs layer is possible to adjust the band alignment between ZnO nanorods and CdS QDs. To reveal this effect, we use UPS technique to analyze the variation of energy level before and after 3-PPA deposition on the surface of ZnO nanorod. Measurements with the UPS were conducted in ultra-high vacuum (UHV) at ~10–10 mbar, by irradiating with 21.22 eV photons(He I line). For each sample, the work function is calculated from the UPS spectrum by subtracting the energy of the incident beam from the difference between the Fermi edge and the low-energy cut-off of secondary electrons (spectrum "width") [60–62]. This technique yields the minimum absolute value of the work function of the surface under examination, and is independent of any experimental parameters, except for the photon energy of the UV source [60–62].

Fig. 8(a) and (b) shows the typical He I UPS spectra for ZnO and 3-PPA(10 mM, 1 min)/ZnO samples in kinetic energy scale. Fig. 8(c) schematically shows the corresponding locations of occupied and unoccupied electronic energy levels near the Fermi level (E_F) for both samples as deduced from the UPS spectra. The location of the Fermi level relative to the vacuum level ($E_{vac} - E_F$), can be determined from the Einstein photoelectric law, as shown following relationship: [63]

$$h\nu = E_{cutoff} + E_{vac} - E_F \quad (1)$$

where E_{cutoff} is the location of the inelastic cutoff and $h\nu$ is the incident photon energy.

The actual positions of E_{cutoff} are determined as the center of the slopes as indicated with vertical lines in Fig. 8(a). Here we would like to point out that, ideally, the edges of UPS spectra should be infinitely abrupt, but they are broadened due to the limited spectrometer resolution and thermal effects [64]. For ZnO, we can obtained the $E_{vac} - E_F$ = 4.71 eV since the E_{cutoff} is 16.51 eV as indicated in Fig. 8(a). The location of the valence band maximum (E_{VBM}) can be determined by choosing the point of maximum inaction near E_F. Then we can obtain the $E_F - E_{VBM}$ = 2.07 eV, as indicated in Fig. 8(a). The ionization potential (IP) is the location of the valence band maximum (E_{VBM}) relative to E_{vac} so that we can deduce that the IP of ZnO is 6.78 eV. Finally, the electron affinity (EA) is the location of the conduction band minimum (E_{CBM}) relative to the vacuum level. Since UPS only probes occupied states, E_{CBM} cannot

Table 3
Photovoltaic parameters obtained from the *I–V* curves of three 3-PPA(10 mM, 1 min)/ZnO solar cells.

Photoelectrodes	J_{sc} (mA/cm^2)	V_{oc} (V)	*FF*	η (%)
S-1	6.01	0.681	0.332	1.36
S-2	5.94	0.678	0.340	1.37
S-3	5.90	0.682	0.333	1.34

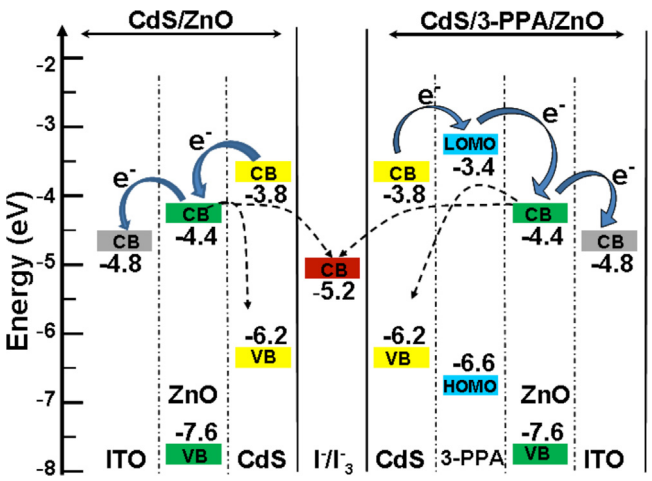

Fig. 9. Energy level diagram for the CdS/ZnO and CdS/3-PPA/ZnO solar cells.

be determined from the UPS spectrum. We utilized the energy band gap (E_g) determined from UV–vis absorption measurements [59]. Since the E_g for ZnO is 3.17 eV as deduced from absorption spectra (Fig. S1), the EA can be deduced to be 3.61 eV. In a similar manner, for 3-PPA(10 mM, 1 min)/ZnO as shown in Fig. 8(b), we can deduce that the E_{cutoff} = 18.96 eV, $E_{vac} - E_F$ = 2.26 eV, $E_F - E_{HOMO}$ = 3.48 eV, IP = 5.74 eV and EA is 2.57 eV. Obviously, we can see that the EA of 3-PPA(10 mM, 1 min)/ZnO is increased by 1.04 eV than that of ZnO. Thus, in Fig. 8(c), the LOMO and HOMO of 3-PPA increase 1.04 eV than the E_C and E_V of ZnO.

Fig. 9 showed the energy level diagram for the CdS/ZnO and CdS/3-PPA/ZnO solar cells. The recombination process of the electrons injected into the conduction band of ZnO nanorod with either the excited CdS or the redox electrolyte I^{3-} is considered as one of the most important factors to determine the short-circuit current density in the photoanode for QDSSCs [65]. Before depositing 3-PPA on the surface of ZnO, the electronic transmission path is the process from CdS to ZnO, then from ZnO to ITO. Since we used the liquid polyiodide as electrolyte, which is fully covered the CdS and ZnO, it will make the photogenerated electrons in the ZnO and CdS recombine with I^{3-} in the electrolyte and shrink the number of electrons which should be transferred to the ITO, which eventually makes the short circuit current density decrease. After a SAMs layer of 3-PPA was deposited between CdS and ZnO, it can be noticed that the LOMO energy level of the 3-PPA is higher than the conduction bandedge (CB) of CdS and ZnO. That is to say, a energy barrier has been formed between CdS and ZnO caused by 3-PPA SAMs, which is very efficient on retarding the back transfer of electrons.

4. Conclusions

In this work, we introduce a SAMs layer of 3-PPA with a phosphonic acid headgroup and carboxylic acid tailgroups in CdS quantum dots sensitized ZnO solar cells and its effects on the photovoltic performance of solar cells have been investigated in detail. The results reveal that the 3-PPA acted as a barrier layer not only suppress the electron-hole recombination process due to its passivation on the surface defects, but forms an energy barrier to efficiently retard the back transfer of electrons, which finally results in the enhancement of conversion efficiency of solar cells. Obviously, the SAMs of 3-PPA in our case acts the same function as ZnS in the ZnO-based QDSSCs. However, the preparing process for 3-PPA is far simpler than that of ZnS, which is quite beneficial for the large-scale industry producing. Meanwhile, our work may stimulate more theoretical and experimental investigations on the effects of SAMs layer on the QDs sensitized solar cell.

Acknowledgements

The authors would like to acknowledge financial support for this work from National Natural Science Foundation of China (Grant nos. 11204104, 61178074, 61008051, 61308095, 61378085 and 11254001), Program for New Century Excellent Talents in University (no. NCET-13-0824), Program for the Development of Science and Technology of Jilin province (Item nos. 201205078 and 20110415), Twentieth Five-Year Program for Science and Technology of Education Department of Jilin Province (item no. 20140147), National Programs for High Technology Research and Development of China (863) (item no. 2013AA032202), Program for the Master Students' Scientific and Innovative Research of Jilin Normal University (item no. 2013022).

References

[1] S. Sarkar, A. Makhal, K. Lakshman, T. Bora, J. Dutta, S.K. Pal, Dual-sensitization via electron and energy harvesting in CdTe quantum dots decorated ZnO nanorod-based dye-sensitized solar cells, J. Phys. Chem. C 116 (2012) 14248–14256.
[2] S.A. Vanalakar, S.S. Mali, R.C. Pawar, N.L. Tarwal, A.V. Moholkar, J.H. Kim, P.S. Patil, Photoelectrochemical properties of CdS sensitized ZnO nanorod arrays: effect of nanorod length, J. Appl. Phys. 112 (2012) 044302.
[3] R. Vogel, P. Hoyer, H. Weller, Quantum-sized PbS, CdS, Ag_2S, Sb_2S_3, and Bi_2S_3 particles as sensitizers for various nanoporous wide-bandgap semiconductors, J. Phys. Chem. 98 (1994) 3183–3188.
[4] M.T. Trinh, A.J. Houtepen, J.M. Schins, T. Hanrath, J. Piris, W. Knulst, A.P.L.M. Goossens, L.DA. Siebbeles, In spite of recent doubts carrier multiplication does occur in PbSe nanocrystals, Nano Lett. 8 (2008) 1713–1718.
[5] S. Mathew, A. Yella, P. Gao, R. Humphry-Baker, B.F.E. Curchod, N. shari-Astani, I. Tavernelli, U. Rothlisberger Md., K. Nazeeruddin, M. Grätzel, Dye-sensitized solar cells with 13% efficiency achieved through the molecular engineering of porphyrin sensitizers, Nat. Chem. 6 (2014) 242–247.
[6] S. Giménez, I. Mora-Seró, L. Macor, N. Guijarro, T. Lana-Villarreal, R. Gómez, L.J. Diguna, Q. Shen, T. Toyoda, J. Bisquert, Improving the performance of colloidal quantum-dot-sensitized solar cells, Nanotechnology 20 (2009) 295204.
[7] Q. Shen, J. Kobayashi, L.J. Diguna, T. Toyoda, Effect of ZnS coating on the photovoltaic properties of CdSe quantum dot-sensitized solar cells, J. Appl. Phys. 103 (2008) 084304.
[8] I.O. Oladeji, L. Chow, Synthesis and processing of CdS/ZnS multilayer films for solar cell application, Thin Solid Films 474 (2005) 77–83.
[9] Y.F. Sun, J.H. Yang, L.L. Yang, J. Cao, M. Gao, Z.Q. Zhang, Z. Wang, H. Song, Improve the open-circuit voltage of ZnO solar cells with inserting ZnS layers by two ways, J. Solid State Chem. 200 (2013) 258–264.
[10] G. Fichet, N. Corcoran, P.K.H. Ho, A.C. Arias, J.D. MacKenzie, W.T.S. Huck, R.H. Friend, Self-organized photonic structures in polymer light-emitting diodes, Adv. Mater. 16 (2004) 1908–1912.
[11] K.H. Yim, Z.J. Zheng, R.H. Friend, W.T.S. Huck, J.S. Kim, Surface-directed phase separation of conjugated polymer blends for efficient light-emitting diodes, Adv. Funct. Mater. 18 (2008) 2897–2904.
[12] K.Y. Wu, S.Y. Yu, Y.T. Tao, Continuous modulation of electrode work function with mixed self-assembled monolayers and its effect in charge injection, Langmuir 25 (2009) 6232–6238.
[13] S.G.J. Mathijssen, P.A. van Hal, T.J.M. van den Biggelaar, E.C.P. Smits, B. de Boer, M. Kemerink, R.A. Janssen, D.M. de Leeuw, Manipulating the local light emission in organic light-emitting diodes by using patterned self-assembled monolayers, Adv. Mater. 20 (2008) 2703–2706.
[14] D.J. Gundlach, J.E. Royer, S.K. Park, S. Subramanian, O.D. Jurchescu, B.H. Hamadani, A.J. Moad, R.J. Kline, L.C. Teague, O. Kirillov, C.A. Richter, J.G. Kushmerick, L.J. Richter, S.R. Parkin, T.N. Jackson, J.E. Anthony, Contact-induced crystallinity for high-performance soluble acene-based transistors and circuits, Nat. Mater. 7 (2008) 216–221.
[15] X. Bulliard, S.G. Ihn, S. Yun, Y. Kim, D. Choi, J.Y. Choi, M. Kim, M. Sim, J.H. Park, W. Choi, K. Cho, Enhanced performance in polymer solar cells by surface energy control, Adv. Funct. Mater. 20 (2010) 4381–4387.
[16] U. Zschieschang, M. Halik, H. Klauk, Microcontact-printed self-assembled monolayers as ultrathin gate dielectrics in organic thin-film transistors and complementary circuits, Langmuir 24 (2008) 1665–1669.
[17] E.D. Gomez, Y.L. Loo, Engineering the organic semiconductor electrode interface in polymer solar cells, J. Mater. Chem. 20 (2010) 6604–6611.
[18] Q. Miao, M. Lefenfeld, T.Q. Nguyen, T. Siegrist, C. Kloc, C. Nuckolls, Self-assembly and electronics of dipolar linear acenes, Adv. Mater. 17 (2005) 407–412.
[19] M.S. Lim, K. Feng, X.Q. Chen, N.Q. Wu, A. Raman, J. Nightingale, E.S. Gawalt, D. Korakakis, L.A. Hornak, A.T. Timperman, Adsorption and desorption of stearic acid self-assembled monolayers on aluminum oxide, Langmuir 23 (2007) 2444–2452.
[20] D.L. Allara, R.G. Nuzzo, Spontaneously organized molecular assemblies. 1. Formation, dynamics and physical properties of *n*-alkanoic acids adsorbed from solution on an oxidized aluminum surface, Langmuir 1 (1985) 45–52.

[21] Y.T. Tao, Structural comparison of self-assembled, monolayers of *n*-alkanoic acids on the surfaces of silver, copper, and aluminum, J. Am. Chem. Soc. 115 (1993) 4350–4358.
[22] H.I. Kim, T. Koini, T.R. Lee, S.S. Perry, Systematic studies of the frictional properties of fluorinated monolayers with atomic force microscopy: comparison of CF3- and CH3-terminated films, Langmuir 13 (1997) 7192–7196.
[23] H.I. Kim, M. Graupe, O. Oloba, T. Koini, S. Imaduddin, T.R. Lee, S.S. Perry, Molecularly specific studies of the frictional properties of monolayer films: asystematic comparison of CF_3—$(CH_3)_2CH$—, and CH3-terminated films, Langmuir 15 (1999) 3179–3185.
[24] S. Lee, Y.-S. Shon, J.R. Colorado, R.L. Guenard, T.R. Lee, S.S. Perry, The influence of packing densities and surface order on the frictional properties of alkanethiol self-assembled monolayers (SAMs) on gold: a comparison of sams derived from normal and spiroalkanedithiols, Langmuir 16 (2000) 2220–2224.
[25] H.I. Kim, T. Koini, T.R. Lee, S.S. Perry, Molecular contribution to the frictional properties of fluorinated self-assembled monolayers, Tribol. Lett. 4 (1998) 137–140.
[26] P. Wang, C. Klein, R. Humphry-Baker, S.M. Zakeeruddin, M. Gratzel, Stable >8% efficient nanocrystalline dye-sensitized solar cell based on an electrolyte of low volatility, Appl. Phys. Lett. 86 (2005) 123508.
[27] J.S. Kim, J.H. Park, J.H. Lee, J. Jo, D.Y. Kim, K. Cho, Control of the electrode work function and active layer morphology via surface modification of indium tin oxide for high efficiency organic photovoltaics, Appl. Phys. Lett. 91 (2007) 112111.
[28] T.C. Monson, M.T. Lloyd, D.C. Olson, Y.J. Lee, J.W.P. Hsu, Photocurrent enhancement in polythiophene- and alkanethiol-modified ZnO solar cells, Adv. Mater. 20 (2008) 4755–4759.
[29] O. Pachoumi, A.A. Bakulin, A. Sadhanala, H. Sirringhaus, R.H. Friend, Y. Vaynzof, Improved performance of ZnO/polymer hybrid photovoltaic devices by combining metal oxide doping and interfacial modification, J. Phys. Chem. C 118 (2014) 18945–18950.
[30] J. Weickert, E. Zimmermann, J.B. Reindl, T. Pfadler, J.A. Dorman, A. Petrozza, L. Schmidt-Mende, Synergistic effects of interfacial modifiers enhance current and voltage in hybrid solar cells, APL Mater. 1 (2013) 042109.
[31] S. Shao, K. Zheng, K. Zidek, P. Chabera, T. Pullerits, F. Zhang, Optimizing ZnO nanoparticle surface for bulk heterojunction hybrid solar cells, Sol. Energy Mater. Sol. Cells 118 (2013) 43–47.
[32] G.J. Wang, T.G. Jiu, G. Tang, J. Li, P.D. Li, X.J. Song, F.S. Lu, J.F. Fang, Interface modification of ZnO-based inverted PTB7:PC71BM organic solar cells by cesium stearate and simultaneous enhancement of device parameters, ACS Sustainable Chem. Eng. 2 (2014) 1331–1337.
[33] J.E. Baio, C. Jaye, D.A. Fischer, T. Weidner, High-throughput analysis of molecular orientation on surfaces by NEXAFS imaging of curved sample arrays, ACS Comb. Sci. 16 (2014) 449–453.
[34] R. Liu, Z. Zheng, J. Spurgeon, X.G. Yang, Enhanced photoelectrochemical water-splitting performance of semiconductors by surface passivation layers, Energy Environ. Sci. 7 (2014) 2504–2517.
[35] S.I. Yoo, T. TrangDo, Y.E. Ha, M.Y. Jo, J. Park, Y.-C. Kang, J.H. Kim, Effect of self-assembled monolayer treated ZnO on the photovoltaic properties of inverted polymer solar cells, Bull. Korean Chem. Soc. 35 (2014) 569–574.
[36] J.Y. Zou, C.Z. Li, C.-Y. Chang, H.-L. Yip, A.K.-Y. Jen, Interfacial engineering of ultrathin metal film transparent electrode for flexible organic photovoltaic cells, Adv. Mater. 26 (2014) 3618–3623.
[37] S.R. Cowan, P. Schulz, A.J. Giordano, A. Garcia, B.A. MacLeod, S.R. Marder, A. Kahn, D.S. Ginley, E.L. Ratcliff, D.C. Olson, Chemically controlled reversible and irreversible extraction barriers via stable interface modification of zinc oxide electron collection layer in polycarbazole-based organic solar cells, Adv. Funct. Mater. 24 (2014) 4671–4680.
[38] Y.-M. Sung, F.-C. Hsu, Y.-F. Chen, Improved charge transport in inverted polymer solar cells using surface engineered ZnO-nanorod array as an electron transport layer, Solar Energy Mater. Solar Cells 125 (2014) 239–247.
[39] Y.E. Ha, M.Y. Jo, J. Park, Y.-C. Kang, S.-J. Moonc, J.H. Kim, Effect of self-assembled monolayer treated ZnO as an electron transporting layer on the photovoltaic properties of inverted type polymer solar cells, Synth. Met. 187 (2014) 113–117.
[40] P.D. Li, X.F. Li, C.M. Sun, G.J. Wang, J. Li, T.G. Jiu, J.F. Fang, Performance enhancement of inverted polymer solar cells with fullerene ester derivant-modified ZnO film as cathode buffer layer, Solar Energy Mater. Solar Cells 126 (2014) 36–41.
[41] I. Mora-Seró, J. Bisquert, Breakthroughs in the development of semiconductor sensitized solar cells, J. Phys. Chem. Lett. 1 (2010) 3046–3052.
[42] V. Gónzalez-Pedro, X.Q. Xu, I. Mora-Seró, J. Bisquert, Modeling high-efficiency quantum dot sensitized solar cells, ACS Nano 4 (2010) 5783–5790.
[43] M. Shalom, S. Ruhle, I. Hod, S. Yahav, A. Zaban, Energy level alignment in CdS quantum dot sensitized solar cells using molecular dipoles, J. Am. Chem. Soc. 131 (2009) 9876–9877.
[44] Y.L. Lee, B.M. Huang, H.T. Chien, Highly efficient CdS sensitized TiO_2 photoelectrode for quantum-dot-sensitized solar cell applications, Chem. Mater. 20 (2008) 6903–6905.
[45] P. Ardalan, T.P. Brennan, H.-B.-R. Lee, J.R. Bakke, I.-K. Ding, M.D. McGehee, S.F. Bent, Effects of self-assembled monolayers on solid-state CdS quantum dot sensitized solar cells, ACS Nano 5 (2011) 1495–1504.
[46] S. Pawsey, K. Yach, L. Reven, Self-assembly of carbox-yalkylphosphonic acids on metal oxide powders, Langmuir 18 (2002) 5205–5212.
[47] J.P. Folkers, C.B. Gorman, P.E. Laibinis, G.M. Whitesides, R.G. Nuzzo, Self-assembled monolayers of long-chain hydroxamic acids on the native oxide of metals, Langmuir 11 (1995) 813–824.
[48] L.L. Yang, Q.X. Zhao, M. Willander, Size-controlled growth of well-aligned ZnO nanorod arrays with two-step chemical bath deposition method, J. Alloy. Compd. 469 (2009) 623–629.
[49] L.L. Yang, Q.X. Zhao, M. Willander, J.H. Yang, Effective way to control the size of well-aligned ZnO nanorod arrays withtwo-step chemical bath deposition, J. Cryst. Growth 311 (2009) 1046–1050.
[50] Q.X. Zhao, L.L. Yang, M. Willander, B.E. Sernelius, P.O. Holtz, Surface recombination in ZnO nanorods grown by chemical bath deposition, J. Appl. Phys. 104 (2008) 073526.
[51] D.D. Wang, J.H. Yang, G.Z. Xing, L.L. Yang, J.H. Lang, M. Gao, B. Yao, T. Wu, Abnormal blueshift of UV emission in single-crystalline ZnO nanowires, J. Lumin. 129 (2009) 996–999.
[52] L.L. Yang, Q.X. Zhao, M. Willander, X.J. Liu, M. Fahlman, J.H. Yang, Origin of the surface recombination centers in ZnO nanorods arrays by X-ray photoelectron spectroscopy, Appl. Surf. Sci. 256 (2010) 3592–3597.
[53] H. Liu, Q. Gao, P. Dai, J.C. Zhang, I. Zhang, N. Bao, Preparation and characterization of activated carbon from lotus stalk with guanidine phosphate activation: sorption of Cd(II), J. Anal. Appl. Pyrol. 102 (2013) 7–15.
[54] B.B. Zhang, T. Kong, W.Z. Xu, R.G. Su, Y.H. Gao, G.S. Cheng, Surface functionalization of zinc oxide by carboxyalkylphosphonic acid self-assembled monolayers, Langmuir 26 (2010) 4514–4522.
[55] E. Smecca, A. Motta, M.E. Fragalà, Y. Aleeva, G.G. Condorelli, Spectroscopic and theoretical study of the grafting modes of phosphonic acids on ZnO nanorods, J. Phys. Chem. C 117 (2013) 5364–5372.
[56] U. Dembereldorj, E.O. Ganbold, J.H. Seo, S.Y. Lee, S.I. Yang, S.W. Joo, Conformational changes of proteins adsorbed onto ZnO nanoparticle surfaces investigated by concentration-dependent infrared spectroscopy, Vib. Spectrosc. 59 (2012) 23–28.
[57] R. Luschtinetz, G. Seifert, E. Jaehne, H.J.P. Adler, Infrared spectra of alkylphosphonic acid bound to aluminium surfaces, Macromol. Symp. 254 (2007) 248–253.
[58] L.L. Yang, Q.X. Zhao, M. Willander, J.H. Yang, I. Ivanov, Annealing effects on optical properties of low temperature grown ZnO nanorod arrays, J. Appl. Phys. 105 (2009) 053503.
[59] L.L. Yang, Z.Q. Zhang, J.H. Yang, Y.S. Yan, Y.F. Sun, J. Cao, M. Gao, M.B. Wei, J.H. Lang, F.Z. Liu, Z. Wang, Effect of tube depth on the photovoltaic performance of CdS quantum dots sensitized ZnO nanotubes solar cells, J. Alloy. Compd. 543 (2012) 58–64.
[60] J.S. Kim, B. Lägel, E. Moons, N. Johansson, I.D. Baikie, W.R. Salaneck, R.H. Friend, F. Cacialli, Kelvin probe and ultraviolet photoemission measurements of indium tin oxide work function: a comparison, Synthetic Met. 111–112 (2000) 311–314.
[61] G. Ertl, J. Kuppers, Low-Energy Electrons and Surface Chemistry, VCH, Weinheim, 1985.
[62] M. Cardona, L. Ley, Photoemission in Solids I, Springer-Verlag, New York, NY, 1978.
[63] Y. Park, Y. So, S.J. Chung, J.I. Jin, Photoelectron spectroscopy study of the electronic structures of poly(*p*-phenylenevinylene) derivatives, J. Korean Phys. Soc. 37 (2000) 59–63.
[64] Y. Park, V. Choong, Y. Gao, B.R. Hsieh, C.W. Tang, Work function of indium tin oxide transparent conductor measured by photoelectron spectroscopy, Appl. Phys. Lett. 68 (1996) 2699–2701.
[65] L.Z. Liu, Y.Q. Chen, T.B. Guo, Y.Q. Zhu, Y. Su, C. Jia, M.Q. Wei, Y.F. Cheng, Chemical conversion synthesis of ZnS shell on ZnO nanowire arrays: morphology evolution and its effect on dye-sensitized solar cell, ACS Appl. Mater. Interfaces 4 (2012) 17–23.